

Large anomalous Hall effect observed in the cubic-lattice antiferromagnet Mn_3Sb with kagome lattice

Hiroaki Hayashi,^{1,2} Yuichi Shirako,¹ Lei Xing,¹ Alexei A. Belik¹, Masao Arai³, Masanori Kohno,¹ Taichi Terashima¹, Hiroshi Kojitani,⁴ Masaki Akaogi⁴, and Kazunari Yamaura^{1,2,*}

¹Research Center for Materials Nanoarchitectonics (MANA), National Institute for Materials Science, 1-1 Namiki, Tsukuba, Ibaraki 305-0044, Japan

²Graduate School of Chemical Sciences and Engineering, Hokkaido University, North 10 West 8, Kita-ku, Sapporo, Hokkaido 060-0810, Japan

³Center for Basic Research on Materials, National Institute for Materials Science, 1-1 Namiki, Tsukuba, Ibaraki 305-0044, Japan

⁴Department of Chemistry, Faculty of Science, Gakushuin University, 1-5-1 Mejiro, Toshima-ku, Tokyo 171-8588, Japan



(Received 13 June 2023; revised 12 July 2023; accepted 31 July 2023; published 17 August 2023)

The anomalous Hall effect, typically observed in ferromagnetic metals, can also manifest in certain noncollinear antiferromagnetic materials. However, studying the cubic kagome antiferromagnet Mn_3X ($X = \text{Ir}, \text{Pt}, \text{Rh}$), which was theoretically predicted to exhibit the anomalous Hall effect, has proven challenging due to the extremely small measured values. In this study, we validate these theoretical predictions by successfully measuring a remarkable anomalous Hall conductivity in the cubic kagome antiferromagnet Mn_3Sb , reaching up to $308 \Omega^{-1} \text{cm}^{-1}$. Combining these results with those obtained from the hexagonal kagome antiferromagnet Mn_3Z ($Z = \text{Sn}, \text{Ge}$), our findings contribute to a comprehensive understanding of the anomalous Hall effect in noncollinear antiferromagnetic materials, leading to further advancements in the research on the functions and control of cluster multipoles.

DOI: [10.1103/PhysRevB.108.075140](https://doi.org/10.1103/PhysRevB.108.075140)

I. INTRODUCTION

The anomalous Hall effect (AHE) is a phenomenon commonly observed in ferromagnetic (FM) metals, but it can also manifest in certain noncollinear antiferromagnetic (AFM) materials [1–4]. One such example is hexagonal Mn_3Z ($Z = \text{Sn}, \text{Ge}$), which exhibits a pronounced AHE comparable to that observed in FM metals [5–8]. In these materials, noncollinear 120° magnetic structures of a two-dimensional kagome lattice are stacked along a particular crystallographic direction [5–8]. The materials with this specific magnetic system are defined in this report as kagome antiferromagnets. Extensive investigations of the topological properties of these kagome antiferromagnets have been carried out using first-principles calculations [9,10]. Theoretical proposals have also highlighted the spin-polarized nature of charge flow in hexagonal Mn_3Z , thereby instigating expectations for spintronic-device applications [11,12]. The substitution of conventional FM metals with AFM metals in spintronic devices offers promising technological advantages. These include the potential for ultrafast switching of magnetic moments, rapid spin response (100–1000 times faster than FM materials), absence of magnetic field leakage (beneficial for high device densities), and resistance to magnetic field disturbances. Consequently, there has been a notable increase in research activities dedicated to exploring these possibilities [7,11,12].

The AHE arises from a combination of time-reversal symmetry breaking and the specific magnetic structure of a material. In FM states with collinear magnetization, the AHE

requires the presence of spin-orbit coupling (SOC) [1]. However, in noncoplanar AFM states, the AHE can emerge even without SOC, thanks to the presence of scalar spin chirality. The latter may be closely associated with the topological Hall effect, while the former has been extensively studied [1–3,13]. In the case of hexagonal Mn_3Z ($Z = \text{Sn}, \text{Ge}$), the contribution of macroscopic quantities such as uniform magnetization and scalar spin chirality to the observed AHE is still a topic of ongoing debate. The interplay between these factors and their role in determining the AHE in AFM systems remains an active area of research.

Recent cluster-multipole (CMP) theory predicts that the coplanar antiferromagnet Mn_3X ($X = \text{Ir}, \text{Pt}, \text{Rh}$) should exhibit the AHE [14]. Specifically, the cubic kagome antiferromagnet Mn_3Ir , commonly used in spin-valve devices, is theoretically expected to display significant anomalous Hall conductivity [10,15]. However, experimental observations of Mn_3Ir have only yielded values approximately one-tenth of the predicted values [16–18]. Similarly, Mn_3Rh , sharing the same kagome lattice, does not exhibit the AHE, and Mn_3Pt shows significantly smaller measured values [17]. Several factors could contribute to this discrepancy between theory and experiment for cubic kagome antiferromagnet Mn_3X . For example, unassessed impurity scattering and lattice disorders might complicate the experimental observations. Additionally, strong magnetic anisotropy may make it difficult to align domains, resulting in the cancellation of the local AHE signal during experimental measurements [16–18]. Furthermore, the difference in coplanar AFM spin structures between cubic Mn_3X ($X = \text{Ir}, \text{Pt}, \text{Rh}$) and hexagonal Mn_3Z ($Z = \text{Sn}, \text{Ge}$) could also be relevant, as the significant AHE is observed only in the latter [19], although recent CMP theory does not

*YAMAURA.Kazunari@nims.go.jp

distinguish between them in terms of the emergence of AHE [14]. Despite considering these factors, the experimental underestimation of the AHE values for cubic kagome antiferromagnet Mn_3X remains incompletely understood.

This study aims to investigate the AHE in both cubic and hexagonal antiferromagnets Mn_3Sb . Surprisingly, a large AHE was observed in the cubic antiferromagnet Mn_3Sb , while no AHE was detected in the hexagonal antiferromagnet Mn_3Sb , deviating from the general trend observed thus far. The significant anomalous Hall conductivity observed in cubic Mn_3Sb is an angle-averaged value in polycrystals, but it is comparable to the theoretical values calculated from Berry curvature. Therefore, the absence of a large AHE in cubic kagome antiferromagnet Mn_3X ($X = \text{Ir}, \text{Pt}, \text{Rh}$), other than Mn_3Sb , may be attributed to individual material-specific factors that are difficult to accurately assess. These findings contribute significantly to advancing the comprehensive understanding of the underlying physics governing the AHE in noncollinear AFM materials.

II. EXPERIMENT

A. Materials preparation

Referring to the binary phase diagram of Mn-Sb, it is evident that only Mn_2Sb and $\text{Mn}_{1.1}\text{Sb}$ are stable, with no other binary alloys present [20]. Therefore, it is believed that cubic Mn_3Sb did not exist until its synthesis by Yamashita *et al.* using a high-pressure method in 2003 [21,22]. In this study, we successfully synthesized cubic Mn_3Sb under similar conditions. Furthermore, we expanded the synthesis pressure range up to 15 GPa and successfully synthesized hexagonal Mn_3Sb .

We synthesized cubic Mn_3Sb under high-pressure conditions (6 GPa, 850 °C) using a multianvil press (CTF-MA1500P, C&T Factory, Tokyo, Japan). Furthermore, employing a Kawai-type press at Gakushuin University (UHP-1000, Sumitomo Heavy Industries, Ltd., Tokyo, Japan), we expanded the synthesis pressure range up to 15 GPa and successfully synthesized hexagonal Mn_3Sb (15 GPa, 1000 °C). The samples were sintered polycrystals, and no single crystals were obtained.

The starting materials used for the synthesis of both cubic and hexagonal Mn_3Sb were 10 wt.% excess Mn powder (99.9%, Aldrich) and Sb powder (99.9%, Rare Metal). The Mn powder was pretreated in a hydrogen atmosphere, but it was not possible to completely remove MnO in our laboratory. The Sb powder was used as purchased from the manufacturer without any prior heat treatment. Although a small amount of MnO was detected in the samples, we considered the effect on the physical property measurement to be small since MnO is a Néel temperature 116 K antiferromagnetic material that is electrically insulating and does not have magnetic order at room temperature [23].

Finely ground powders of both alloys were utilized in synchrotron x-ray-diffraction (XRD) experiments at temperatures ranging from 100 to 400 K. The XRD measurements were conducted using a large Debye-Scherrer camera at the BL02B2 beamline at SPring-8, Sayo, Japan [24,25]. The synchrotron XRD wavelength used was either 0.420 26 or

0.77598 Å, and it was calibrated using CeO_2 as the standard material. The difference in wavelength was not based on any scientific rationale but rather on practical considerations we encountered. The synchrotron XRD data were analyzed using the Rietveld method [26] with RIETAN-FP software [27].

B. Magnetic and transport properties measurements

The direct-current magnetic susceptibilities of the alloys were measured using a superconducting quantum interference device magnetometer (MPMS, Quantum Design, San Diego, CA, USA). The measurements were performed in the temperature range of 2–550 K using an oven (300–550 K) and an applied magnetic field of 1 T, under both zero-field-cooled (ZFC) and field-cooled (FC) conditions. Isothermal magnetization loops were collected at different temperatures within the magnetic field range of ± 1 T.

The electrical resistivity (ρ_{xx}) and Hall resistivity (ρ_{xy}) of a polycrystalline material were measured as a function of temperature and magnetic field using a conventional low-frequency alternating-current four-probe method in a ^4He variable temperature insert with a superconducting magnet. Au wires were spot welded and reinforced with silver paste for electrical contacts on the plate-shaped material. To ensure accurate measurements, both positive and negative magnetic fields were applied to eliminate any mixing of ρ_{xx} and ρ_{xy} . The experimental signals, $\rho_{xx-\text{exp}}$ and $\rho_{xy-\text{exp}}$, were symmetrized and antisymmetrized to obtain the true ρ_{xx} and ρ_{xy} , respectively. Specifically, $\rho_{xx}(H) = [\rho_{xx-\text{exp}}(H) + \rho_{xx-\text{exp}}(-H)]/2$, and $\rho_{xy}(H) = [\rho_{xy-\text{exp}}(H) - \rho_{xy-\text{exp}}(-H)]/2$.

C. Theoretical calculations

First-principles calculations of cubic Mn_3Sb and its related materials were carried out using the projector augmented-wave method within the Vienna *ab initio* Simulation Package (VASP) [28]. The calculations employed the generalized gradient approximation (GGA) of density-functional theory with the Perdew-Burke-Ernzerhof exchange functional [29]. Structure optimizations were performed using an $8 \times 8 \times 8$ uniform k -point grid, and Gaussian broadening with a width of 0.1 eV was applied. The final electronic structure was obtained using tetrahedron methods. Maximally localized Wannier functions [30,31] were then constructed using the WANNIER90 program package [32]. The anomalous Hall conductivity was calculated based on the Berry curvature [1] of the energy bands derived from the tight-binding model using the Wannier functions [10,15,33].

The intrinsic anomalous Hall conductivity was determined using the Berry curvature method. Initially, the maximally localized Wannier functions (MLWFs) were generated using the WANNIER90 program code [32], utilizing the energy bands obtained from *ab initio* calculations for the experimental structure. A total of 144 energy bands located above EF-8 eV were employed as input for WANNIER90, where EF represents the Fermi energy. The s , p , and d projectors were utilized for all atoms. To ensure disentanglement [32], the energy range from EF-8 to EF + 1.8 eV was selected as the frozen energy region. Subsequently, a tight-binding model was constructed based on the MLWFs. The Berry curvature was then computed

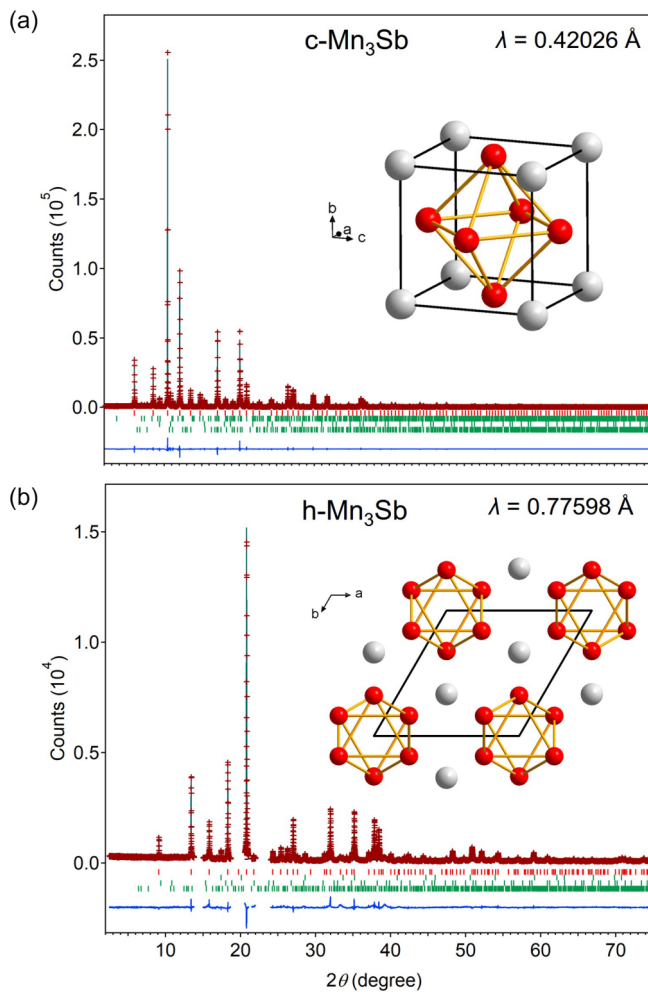


FIG. 1. Synchrotron XRD patterns of cubic and hexagonal Mn_3Sb at room temperature, showing observed (crosses) and calculated (solid red lines) patterns. Differences are shown as solid blue lines at bottom. Bragg reflections are indicated by vertical ticks, with upper row representing main phase reflections (red) and lower row representing impurity phase reflections (green). Impurity phases include MnO (6.7 wt.%), Mn_2Sb (2.3 wt.%), and Sb (1.3 wt.%) for cubic Mn_3Sb , and MnO and unidentified phases for hexagonal Mn_3Sb . Unit cells are shown as insets, with Mn and Sb denoted by red and gray balls, respectively.

for this tight-binding model, employing an adaptive k -point mesh of up to $200 \times 200 \times 200$. The specific configuration of the adaptive k -point mesh [32] chosen was $5 \times 5 \times 5$.

III. RESULTS

A. Crystal structure

We investigated the crystal structures of Mn_3Sb in cubic and hexagonal phases using synchrotron XRD data and Rietveld refinement methods. The results are shown in Figs. 1(a) and 1(b). First, we focused on the analysis of the cubic Mn_3Sb . Based on the structural model of Mn_3Sb synthesized under high-pressure conditions reported in 2003 [21], we attempted to refine the structure using a cubic-ordered model ($Pm\bar{3}m$). We also examined a disordered model, such as that observed

in $\text{Mn}_{2.8}\text{Ir}_{1.2}$ ($Pm\bar{3}m$) [34], but in this study, analysis using a perfectly ordered model was found to be optimal. Ultimately, the analysis proceeded with a complete occupancy for each site of Mn and Sb atoms. The obtained structural parameters yielded reasonable values, as summarized in Table I. A structural image of the cubic Mn_3Sb was drawn based on these results and is presented as an inset in Fig. 1(a).

In this study, it was not possible to directly reference past models for hexagonal Mn_3Sb as there were no examples available. Therefore, structural models of Mn_3Sn and Mn_3Ge were referred to Refs. [35–37]. In previous studies of the hexagonal model ($P6_3/mmc$), structures with disorders, including antisite disorder, were observed. However, during the preliminary analysis of our sample, the degree of disorder was estimated to be quite small. Therefore, in the final analysis, an ordered structure model with no antisite disorder was assumed, and all element occupancy factors were set to 1. Despite this assumption, we believe that reasonable results were obtained. Therefore, we conclude that hexagonal Mn_3Sb has the same type of structure as Mn_3Sn and Mn_3Ge , and the degree of disorder in the arrangement of elements can be quite small. The x-ray diffraction pattern of the analyzed hexagonal Mn_3Sb is shown in Fig. 1(b), and detailed crystallographic data are presented in Table I. A structural image drawn based on the parameters obtained here is also shown as an inset figure.

In addition, synchrotron XRD patterns were collected at various temperatures ranging from 100 to 500 K to investigate the temperature dependence of the structural properties of Mn_3Sb in cubic and hexagonal phases. However, no changes in symmetry or additional features were observed. Only monotonic changes in the structural parameters were observed in response to temperature variations (see Supplemental Material, Fig. S1 [38]). Magnetic measurements taken at high temperatures, which will be discussed later, suggested signs of thermal decomposition above 400 K. However, even at temperatures above 400 K, the synchrotron XRD studies did not observe complete decomposition.

B. Magnetization

We investigated the magnetic properties of both cubic and hexagonal Mn_3Sb . Figure 2(a) shows the temperature dependence of the magnetic susceptibility of cubic Mn_3Sb at an applied magnetic field of 1 T. As the magnetic transition temperature exceeded 300 K, we employed the oven mode of MPMS3 for the measurements. However, we were unable to determine the precise transition temperature due to the partial decomposition around 450 K. This phenomenon has been reported in prior studies [39]. Therefore, we could only conclude that the magnetic transition temperature of cubic Mn_3Sb was higher than the thermal decomposition temperature of 450 K. Similarly, the magnetic transition temperature of hexagonal Mn_3Sb could not be precisely determined due to the partial decomposition [Fig. 2(b)]. We just found that the magnetic transition temperature was higher than the thermal decomposition temperature of approximately 420 K. The remarkable upturn observed at high temperatures may be attributed to the formation of MnSb , which is FM and has a Curie temperature of ~ 550 K [40,41].

TABLE I. Atomic positions, occupancies, and thermal displacement parameters of cubic and hexagonal Mn₃Sb obtained using synchrotron XRD.

Mn ₃ Sb	Atom	Site	<i>x</i>	<i>y</i>	<i>z</i>	Occupancy	<i>B</i> _{iso} (Å ²)
Cubic ^a	Mn	3 <i>c</i>	0	0.5	0.5	1	0.491(4)
	Sb	1 <i>a</i>	0	0	0	1	0.366(5)
Hexagonal ^b	Mn	6 <i>h</i>	0.161 17(13)	0.322 35 (= 2 <i>x</i>)	0.25	1	0.503(18)
	Sb	2 <i>d</i>	0.333 33	0.666 67	0.75	1	0.184(16)

^aSpace group: *Pm-3m* (No. 221). *A* = 3.99744(1) Å, *V* = 63.8773(4) Å³, and *Z* = 1. *D*_{cal} = 7.461 g/cm³; Residuals: *R*_{wp} = 7.18%, *R*_p = 5.23%, *S* = 2.33; Mass fractions of Mn₃Sb, MnO, Mn₂Sb, and Sb were 0.897, 0.067, 0.023, and 0.013, respectively; Sample temperature was 296 K.

^bSpace group: *P6₃/mmc* (No. 194). *a* = 5.63434(9) Å, *c* = 4.53434(6) Å, *V* = 124.661(3) Å³, and *Z* = 2. *d*_{cal} = 7.635 g/cm³; Residuals: *R*_{wp} = 10.94%, *R*_p = 8.14%, *S* = 1.60; Mass fractions of Mn₃Sb and MnO other than unknown phase were 0.943 and 0.057, respectively; Sample temperature was 300 K.

In the cubic Mn₃Sb, a divergence between the ZFC and FC curves was observed at temperatures below 25 K. This divergence may indicate the formation of magnetic domains related to the thermal history. However, more precise studies are necessary to accurately assess this possibility.

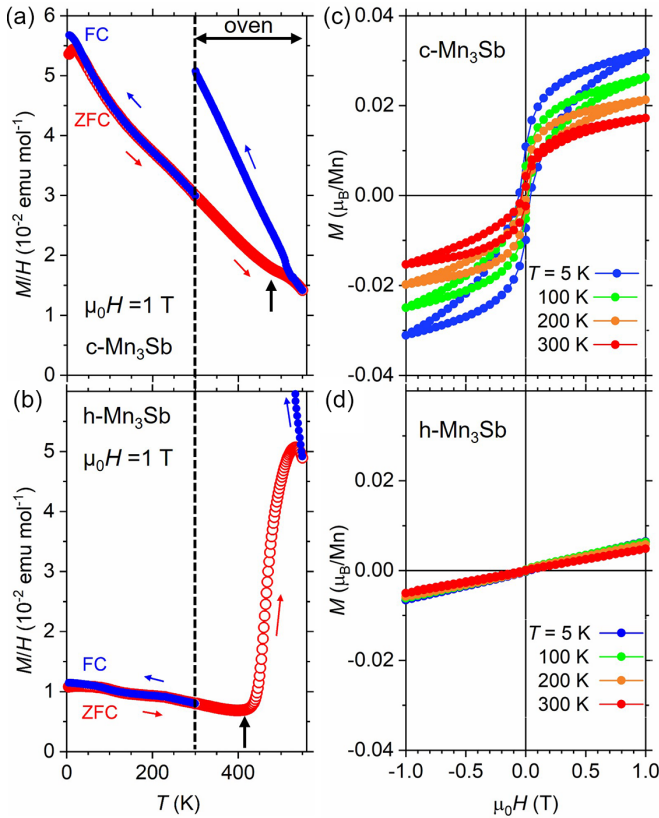


FIG. 2. (a) Temperature dependence of magnetic susceptibility measured at $\mu_0 H = 1$ T. (b) Isothermal magnetization curves at various temperatures for cubic Mn₃Sb. For clarity, some curves are omitted (full version is available in Fig. S2). (c) Temperature dependence of magnetic susceptibility and (d) isothermal magnetization curves for hexagonal Mn₃Sb. Measurements were carried out using oven mode of MPMS3 for temperatures above 300 K. Black arrow denotes temperature at which Mn₃Sb partially decomposes into Mn₂Sb and Mn.

Figures 2(c) and 2(d) summarize the results of measuring the magnetic field dependence of the magnetization of cubic and hexagonal Mn₃Sb at various temperatures, respectively. The magnetization of cubic Mn₃Sb shows hysteresis loops from low temperatures to room temperature, but the magnitude is quite small, with a residual magnetization ($\mu_0 H = 0$) of about $0.004 \mu_B/\text{Mn}$ at 300 K. Therefore, it is not FM or ferrimagnetic, but rather close to characteristics of antiferromagnetism. It is thought that a slight spontaneous magnetization was observed because the AFM cancellation was not complete. On the other hand, the magnetic field dependence of the magnetization of hexagonal Mn₃Sb is very linear regardless of temperature and behaves like typical antiferromagnetism. The measurement result of hexagonal Mn₃Sb is qualitatively different from that of Mn₃Sn with the same crystal structure, showing a small residual magnetization and hysteresis loop.

C. Transport properties

Figure 3(a) shows the temperature dependence of ρ_{xx} for Mn₃Sb with both cubic and hexagonal structures. Both materials exhibit metallic conduction behavior from 4 to 300 K at $\mu_0 H = 0$ and ± 3 T, despite being sintered bulk materials. The resistivity at room temperature is relatively low, at around $1 \times 10^{-4} \Omega \text{ cm}$, and decreases further as the temperature decreases. Therefore, the impact of grain boundaries and impurities is quite small in the longitudinal direction. Little magnetic field dependence is observed for hexagonal Mn₃Sb, whereas slight magnetic field dependence is observed for cubic Mn₃Sb at low temperatures. The measurement results at 4 K, defined by the magnetic resistivity, $MR(H) = 100 \times [\rho_{xx}(H) - \rho_{xx}(0)] / \rho_{xx}(0)$, are also presented in the figure. Even at $\mu_0 H = 4$ T, the maximum change observed is only -1% , suggesting that the suppression of spin fluctuations in an external magnetic field has only a minor effect on the decrease in magnetic resistivity.

The results of measuring the Hall resistivity at several typical temperatures for cubic and hexagonal Mn₃Sb are shown in Figs. 3(b) and 3(c), respectively. Clear AHE was observed in cubic Mn₃Sb. Since sintered samples were used for both measurements, the dependence on crystal orientation could not be studied. However, at 300 K, the absolute value of the Hall resistivity at zero magnetic field ($\mu_0 H = 0$) was as large as

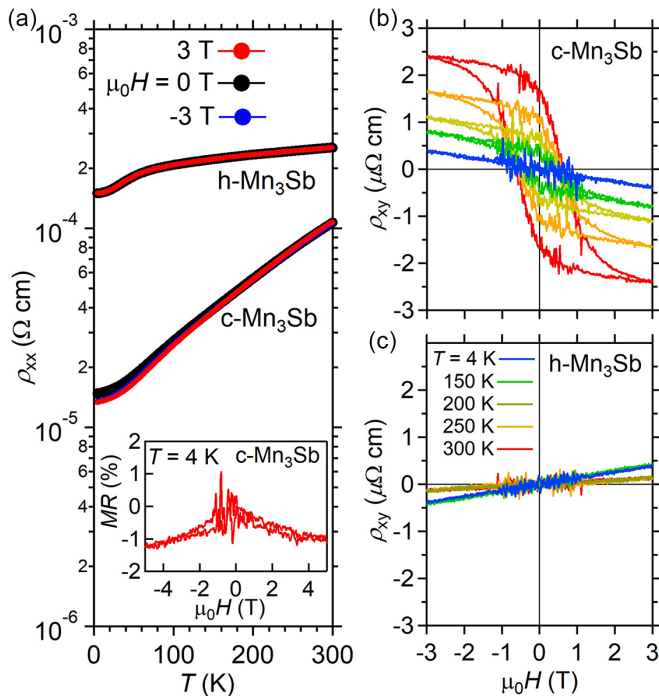


FIG. 3. (a) Temperature dependence of electrical resistivity of cubic and hexagonal Mn_3Sb under various magnetic fields. Inset shows magnetoresistance of cubic Mn_3Sb at 4 K. (b) Hall resistivity of cubic and (c) hexagonal Mn_3Sb at various temperatures. For clarity, some curves for cubic Mn_3Sb are omitted (full version is available in Fig. S3).

$1.68 \times 10^{-6} \Omega \text{ cm}$, which is comparable to that of a FM material [1,42]. Although a direct comparison is difficult due to the difference in measurement conditions (not single-crystal measurements), the value observed in hexagonal Mn_3Sn and Mn_3Ge ($1 \sim 4 \times 10^{-6} \Omega \text{ cm}$) is similar [5–8,43]. In addition, in the measurement of hexagonal Mn_3Sb , which has the same crystal structure as hexagonal Mn_3Sn and Mn_3Ge , no AHE was observed at either low or room temperature [Fig. 3(c)]. Therefore, the AHE in cubic Mn_3Sb is particularly noteworthy. Furthermore, the AHE of cubic Mn_3Sb decreases monotonically with a decrease in sample temperature and is almost eliminated in the measurement at 4 K. Such thermal behavior of AHE is usually not observed in FM materials, indicating that the observed AHE reflects the inherent properties of cubic Mn_3Sb .

D. Magnetic structure

The magnetic structure of cubic Mn_3Sb was initially determined by Ryzhkovskii *et al.* using neutron diffraction in 2011 [39]. However, a subsequent Mössbauer study contradicted the originally proposed collinear AFM spin structure [44]. Instead, the noncollinear triangular AFM model on the kagome lattice, proposed for Mn_3X ($X = \text{Ir}, \text{Pt}, \text{Rh}$), was considered [45–47]. In 2020, the magnetic structure model for cubic Mn_3Sb was revisited, and the triangular AFM model was reintroduced based on neutron-diffraction experiments [48]. Despite the limited clarity in determining the magnetic structure through symmetry analysis of powder neutron-diffraction

TABLE II. Relative total energies (eV/cell) calculated within the GGA + SOC scheme for cubic Mn_3Sb .

Cubic Mn_3Sb	a (Å)	M (μ_B/cell)	ΔE (eV/cell)
Nonmagnetic	3.997 ^a	0	0
Ferromagnetic	3.997 ^a	8.48	-2.08
Collinear AFM	3.997 ^a	2.10	-2.47
Noncollinear AFM	3.997 ^a	~ 0	-2.57
After structure optimization:			
Nonmagnetic	3.742	0	0
Ferromagnetic	3.805	6.07	-1.46
Collinear AFM	3.840	2.06	-1.51
Noncollinear AFM	3.909	~ 0.04	-1.61

^aExperimental value obtained in this study.

In noncollinear antiferromagnetic (AFM) scheme, magnetic moments are oriented triangularly within [111] plane of cubic cell, as proposed in a neutron-diffraction study [48].

data [49], further experimental progress remains challenging. In this study, we reevaluate the proposed magnetic structure models using first-principles calculations.

Table II presents the results of theoretical calculations for the possible magnetic structure models of cubic Mn_3Sb . The collinear AFM model demonstrated in the initial neutron-diffraction experiment was not stable, and the noncollinear AFM structure, as observed in the isostructural cubic Mn_3X ($X = \text{Ir}, \text{Pt}, \text{Rh}$), was found to be the most energetically stable. These theoretical results are consistent with the revisited neutron-diffraction experiments [48]. After optimizing the crystal structure, the numerical results were similar, and the noncollinear AFM model was once again suggested to be the most energetically stable. Attempts were also made to predict the magnitude of magnetization per unit cell using this magnetic structure model. However, technical challenges prevented an accurate quantitative evaluation of the magnitude of magnetization.

The proposed magnetic structure in this study is supported by a combination of experimental evidence from neutron diffraction [48], symmetry analysis [49], Mössbauer spectroscopy [44], first-principles calculations, and magnetization measurements. The nearly coplanar triangular magnetic structure, as shown in the inset of Fig. 4, is highly likely to be the most probable configuration. This magnetic structure model is also consistent with the model observed in Mn_3Ir [34,50]. It is important to note that the magnetic structure of hexagonal Mn_3Sb was not investigated in this study due to a technical difficulty caused by the limited sample quantity (< 10 mg) available for experimental studies.

IV. DISCUSSION

The Hall conductivity (σ_{xy}) of cubic Mn_3Sb was determined after removing the applied magnetic field (> 1 T) using the equation $\sigma_{xy} = -\rho_{xy}/(\rho_{xy}^2 + \rho_{xx}^2)$, where ρ_{xy} is $-1.68 \times 10^{-6} \Omega \text{ cm}$ and ρ_{xx} is $1.07 \times 10^{-4} \Omega \text{ cm}$ (at 300 K with $\mu_0 H = 0$). The calculated value of σ_{xy} is $146 \Omega^{-1} \text{ cm}^{-1}$, which is significantly larger than the room-temperature values of Mn_3Sn ($20 \Omega^{-1} \text{ cm}^{-1}$) [5] and Mn_3Ge ($60 \Omega^{-1} \text{ cm}^{-1}$) [6,7] (see Table III), but comparable to the maximum value of

TABLE III. Comparison of experimentally observed anomalous Hall effects at 298–300 K in cubic Mn_3X and hexagonal Mn_3Z materials. Second-to-last column quantifies anomalous Hall conductivity relative to material's magnetization.

Materials	Space group	T_N (K)	$ \sigma_{xy} (\mu_0H = 0)$ ($\Omega^{-1} \text{cm}^{-1}$)	$M(\mu_0H = 0)$ ($\mu_B \text{ion}^{-1}$)	$ \sigma_{xy} /M_r$ ($10^3 \Omega^{-1} \text{cm}^{-1} \mu_B^{-1} \text{ion}$)	Ref.
Mn_3Ir	$Pm\bar{3}m$ (Cubic)	960 ± 10	2.6/30	0.01	0.3	[16,18,34,47]
Mn_3Pt		473	1.5	0.0003	5	[17,45]
Mn_3Rh		853				[19,46]
Mn_3Ga		400	0	0		[52]
Mn_3Sb		>450	146	0.0032	46	This work
Mn_3Sn	$P6_3/mmc$ (Hexagonal)	430	20	0.003	6.7	[5,7,8,36]
Mn_3Ge		380	60	0.007	8.6	[6,7]
Mn_3Ga		470 ± 10	17	0.07	0.2	[37,43]
Mn_3Sb		>400	0	0		This work

Mn_3Sn ($130 \Omega^{-1} \text{cm}^{-1}$ at 50 K) and approximately 40% of the maximum value of Mn_3Ge ($380 \Omega^{-1} \text{cm}^{-1}$ below 50 K) [6,7]. To compare the AHE of cubic Mn_3X ($X = \text{Ir}, \text{Pt}, \text{Rh}$) that possess the same spin structures, the σ_{xy} at zero magnetic fields ($\mu_0H = 0$) was plotted as a function of temperature in Fig. 4. The value of σ_{xy} increased as the temperature decreased, reaching a peak of approximately $300 \Omega^{-1} \text{cm}^{-1}$ around 150 K. This value significantly surpasses the experimental values observed for other cubic Mn_3X throughout the entire temperature range, whether they are single crystals or polycrystals. It should be noted that the data for Mn_3Sb used in this study are from polycrystalline materials, and the value of σ_{xy} may be somewhat underestimated compared to theoretical values for single-domain crystals due

to angle averaging. However, the observed AHE in polycrystalline Mn_3Sb remains significant and provides valuable information about the AHE behavior in this material.

The observed discrepancy between Mn_3X ($X = \text{Ir}, \text{Pt}, \text{Rh}$) and Mn_3Sb may potentially be attributed to differences in the magnitude of the magnetic anisotropy among these materials, as suggested by thin-film studies on Mn_3Ir [18]. However, even with some alignment of domains at a high magnetic field of 24 T to the Mn_3Ir film, the measured σ_{xy} remains significantly lower than the theoretical value, being an order of magnitude smaller [16].

It is noteworthy that the σ_{xy} of cubic Mn_3Sb gradually decreases below 150 K, unlike the behavior observed in ferromagnets [1] and hexagonal Mn_3Ge [7], which converge to a constant value in the low-temperature limit. In an attempt to elucidate this behavior, we employed the universal scaling approach proposed for magnetic metals (refer to Fig. S4 [38]) [7,51]. The analysis reveals that the anomalous Hall conductivity of cubic Mn_3Sb at around room temperature exhibits a behavior that is highly consistent with the expected properties of the intrinsic AHE, which demonstrates a weak dependence on the longitudinal conductivity. However, the pronounced decrease in anomalous Hall conductivity at low temperatures deviates from universal scaling but still falls within the range of intrinsic behavior. Furthermore, we have carefully examined magnetic susceptibility data and crystal structure parameters, but we have not observed any anomalies that could suggest the causes for the pronounced decrease in σ_{xy} at low temperatures. Additionally, it is worth noting that a significant decrease in σ_{xy} at low temperatures has also been observed in Mn_3Sn , which is associated with a magnetic structure transition. However, neutron-diffraction studies of cubic Mn_3Sb by Ryzhkovski *et al.* did not detect any indications of different magnetic features emerging at 77 K [39,48]. The underlying cause of the decrease in σ_{xy} at low temperatures remains unclear based on our present investigation.

In this study, the anomalous Hall resistivity and remanent magnetization showed continuous variations with temperature (Figs. 2, 3, S2, and S3), without displaying any abrupt changes. To summarize the temperature-dependent behaviors, the anomalous Hall conductivity per remanent magnetization was plotted against temperature, as depicted in Fig. S5 [38]. $|\sigma_{xy}|/M_r = 46000 (\Omega^{-1} \text{cm}^{-1} \mu_B^{-1} \text{ion})$ near room temperature, gradually increased with decreasing temperature,

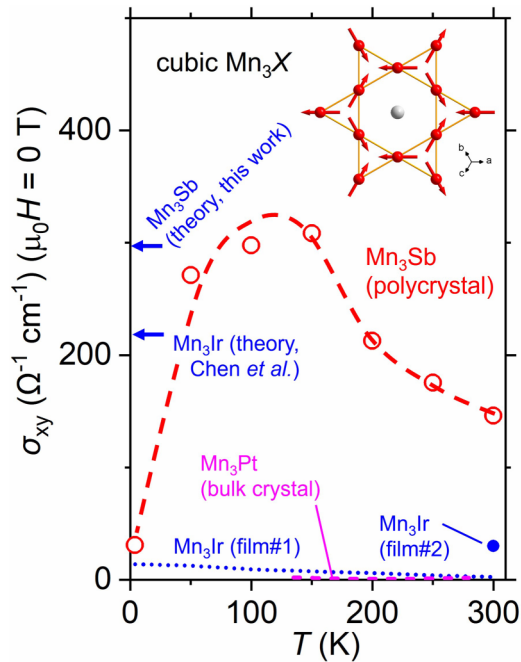


FIG. 4. Temperature dependence of σ_{xy} in polycrystalline cubic Mn_3Sb . Data used for comparison with other isostructural materials were obtained from Refs. [10,16,18] for Mn_3Ir and from Ref. [17] for Mn_3Pt , but unfortunately, experimental data could not be obtained for Mn_3Rh [19]. Inset figure is a schematic of noncollinear AFM structure proposed for Mn_3Sb .

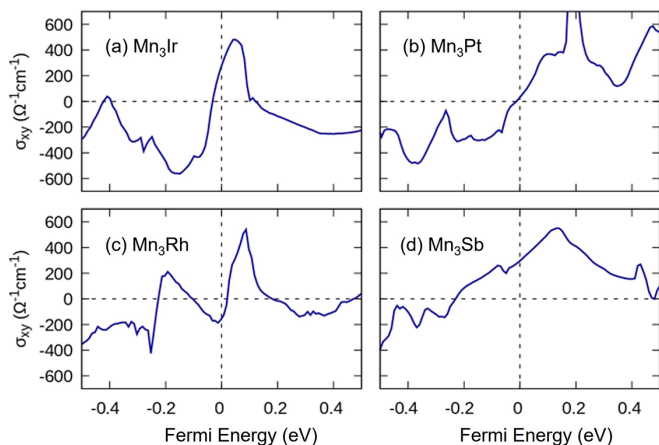


FIG. 5. (a)–(d) Theoretical calculation of anomalous Hall conductivity for cubic Mn_3X ($X = \text{Ir}, \text{Pt}, \text{Rh},$ and Sb) using Wannier functions and Berry curvature.

reaching a maximum at around 150 K, and then exhibited a slow decrease at lower temperatures. No clear abrupt change can be observed, and the underlying reason for the decrease in σ_{xy} at low temperatures still remains unclear. Further analysis of the anomalous Hall conductivity at low temperatures will be necessary in future studies.

The experimental values of σ_{xy} obtained in this study quantitatively agree with the theoretical values calculated from the Berry curvature using the Wannier function for the cubic kagome antiferromagnet Mn_3Sb , as indicated by the arrow in Fig. 4. It should be noted that the data presented in Fig. 4 are angle-averaged values in polycrystals, which may result in some underestimation compared to theoretical values for single-domain crystals due to angular averaging. Nevertheless, the agreement between the experimental and theoretical values provides strong evidence for the presence of a significant anomalous Hall effect in the cubic Mn_3Sb material.

It is worth mentioning that when the same method is applied to the cubic kagome antiferromagnet Mn_3Ir , it accurately reproduces the previously reported theoretical values (the band dispersion for Mn_3Ir is also essentially identical to the previous report, as shown in Fig. S6 [38]) [15]. Moreover, a comparative analysis of the calculated Fermi energy dependence of σ_{xy} between cubic Mn_3Sb and cubic Mn_3Ir (Fig. 5) reveals that σ_{xy} is nearly identical at the Fermi level for both materials. However, the behavior of σ_{xy} in Mn_3Ir exhibits a sharp transition as the Fermi energy varies, while in Mn_3Sb , σ_{xy} changes gradually over a relatively wide range of energy. For instance, in the case of Mn_3Ir , it is predicted that the sign of σ_{xy} will reverse with a decrease in Fermi energy of approximately 0.04 eV. In contrast, for Mn_3Sb , the sign of σ_{xy} is expected to remain unchanged even with a decrease in Fermi energy of 0.2 eV or more. These findings suggest that the anomalous Hall conductivity of cubic Mn_3Sb exhibits greater robustness compared to cubic Mn_3Ir against various perturbations that influence the Fermi energy. This unique characteristic of cubic kagome antiferromagnet Mn_3Sb may prove advantageous for the development of novel AFM spintronic materials, as it indicates a more stable and reliable behavior of the AHE in this compound.

TABLE IV. Comparison of anomalous Hall effects from first-principles calculations in cubic Mn_3X materials.

Materials	σ_{xy} ($\text{cm}^{-1}\Omega^{-1}$) ($z//[111]$)	By Zhang <i>et al.</i> [15]	By Chen <i>et al.</i> [10]
Mn_3Ir	277	312	218
Mn_3Pt	33	98	
Mn_3Rh^a	-152	284	
Mn_3Sb	296		

^aFor Mn_3Rh , calculated value deviates from previous calculations. Deviation could be due to differences in lattice constants or other conditions, as calculated anomalous Hall conductivity is sensitive to position of Fermi energy, as shown in Fig. 5(a).

For comparison, we performed theoretical calculations using the same approach for Mn_3Rh and Mn_3Pt . However, the calculated values of σ_{xy} for these materials are significantly smaller than those for Mn_3Ir and Mn_3Sb (Table IV). Furthermore, the calculated σ_{xy} exhibits a sharp transition near the Fermi energy, indicating their susceptibility to changes in energy. These findings suggest that Mn_3Rh and Mn_3Pt are not as robust as Mn_3Sb in terms of the anomalous Hall conductivity against variations in energy.

V. CONCLUSION

This study has made significant progress in observing the AHE in the cubic kagome antiferromagnet Mn_3Sb . The measured anomalous Hall conductivity of up to $308 \Omega^{-1} \text{cm}^{-1}$ in polycrystalline cubic Mn_3Sb is a remarkable achievement. This value not only agrees well with theoretical calculations based on Berry curvature but also compares favorably to experimental observations in the hexagonal kagome antiferromagnet Mn_3Z ($Z = \text{Sn}, \text{Ge}$). The absence of AHE in the hexagonal Mn_3Sb phase, although not fully understood, does not impact the conclusions drawn in this study. The primary focus of this research is on investigating the AHE in the cubic Mn_3Sb , where significant AHE behavior is observed.

We acknowledge the limitations of comparing AHE and Berry curvature fields in polycrystalline materials. While the anomalous Hall conductivity in polycrystalline materials may be underestimated compared to theoretical values for single-domain crystals due to angular averaging, it still provides important insights into the overall behavior of the AHE. Additionally, we believe Berry curvature calculations offer valuable theoretical insights and help interpret experimental results, even in polycrystalline materials.

We recognize the challenges in accurately determining the contributions of intrinsic and extrinsic factors in polycrystalline materials. The analysis of scaling relations in this study supports the presence of intrinsic AHE in cubic Mn_3Sb , exhibiting the expected behavior with a weak dependence on longitudinal conductivity (Fig. S4). The observed decrease in anomalous Hall conductivity at low temperatures, while deviating from universal scaling, is still within the range of intrinsic behavior. Further investigations will be pursued once single-domain crystals become available to gain a more comprehensive understanding of these phenomena.

These findings demonstrate that the experimental challenges encountered in studying cubic kagome antiferromagnets, such as Mn_3Ir , Mn_3Pt , and Mn_3Rh , are not inherent limitations of the system itself. This contributes to a deeper understanding of the AHE in both cubic kagome antiferromagnets Mn_3X and hexagonal kagome antiferromagnets Mn_3Z , advancing research on the functions and control of cluster multipoles. Furthermore, the substitution of expensive and scarce noble metals Ir, Pt, and Rh with Sb in this study showcases the potential for developing innovative non-collinear AFM spintronic materials.

ACKNOWLEDGMENTS

MANA is supported by the World Premier International Research Center Initiative (WPI) of MEXT, Japan. This research was partly funded by a Grant-in-Aid for Scientific Research from the Japan Society for the Promotion of Science (Grant No. JP22H04601) and the Kazuchika Okura Memorial Foundation (Grant No. 2022-11). Synchrotron radiation was utilized at the powder diffraction beamline BL02B2 at SPring-8, with the permission of the Japan Synchrotron Radiation Research Institute (Proposals No. 2021A1169, No. 2022A1067, No. 2022B1919, and No. 2023A1496).

-
- [1] N. Nagaosa, J. Sinova, S. Onoda, A. H. MacDonald, and N. P. Ong, Anomalous hall effect, *Rev. Mod. Phys.* **82**, 1539 (2010).
- [2] R. Shindou and N. Nagaosa, Orbital Ferromagnetism and Anomalous Hall Effect in Antiferromagnets on the Distorted fcc Lattice, *Phys. Rev. Lett.* **87**, 116801 (2001).
- [3] Y. Taguchi, Y. Oohara, H. Yoshizawa, N. Nagaosa, and Y. Tokura, Spin chirality, Berry phase, and anomalous Hall effect in a frustrated ferromagnet, *Science* **291**, 2573 (2001).
- [4] J. Kübler and C. Felser, Non-collinear antiferromagnets and the anomalous Hall effect, *EPL* **108**, 67001 (2014).
- [5] S. Nakatsuji, N. Kiyohara, and T. Higo, Large anomalous Hall effect in a non-collinear antiferromagnet at room temperature, *Nature (London)* **527**, 212 (2015).
- [6] N. Kiyohara, T. Tomita, and S. Nakatsuji, Giant Anomalous Hall Effect in the Chiral Antiferromagnet Mn_3Ge , *Phys. Rev. Appl.* **5**, 064009 (2016).
- [7] T. Chen, T. Tomita, S. Minami, M. Fu, T. Koretsune, M. Kitatani, I. Muhammad, D. Nishio-Hamane, R. Ishii, F. Ishii, R. Arita, and S. Nakatsuji, Anomalous transport due to weyl fermions in the chiral antiferromagnets Mn_3X , $\text{X} = \text{Sn}, \text{Ge}$, *Nat. Commun.* **12**, 572 (2021).
- [8] Y. Song, Y. Hao, S. Wang, J. Zhang, Q. Huang, X. Xing, and J. Chen, Complicated magnetic structure and its strong correlation with the anomalous Hall effect in Mn_3Sn , *Phys. Rev. B* **101**, 144422 (2020).
- [9] H. Yang, Y. Sun, Y. Zhang, W.-J. Shi, S. S. P. Parkin, and B. Yan, Topological Weyl semimetals in the chiral antiferromagnetic materials Mn_3Ge and Mn_3Sn , *New J. Phys.* **19**, 015008 (2017).
- [10] H. Chen, Q. Niu, and A. H. MacDonald, Anomalous Hall Effect Arising from Noncollinear Antiferromagnetism, *Phys. Rev. Lett.* **112**, 017205 (2014).
- [11] J. Železný, Y. Zhang, C. Felser, and B. Yan, Spin-Polarized Current in Noncollinear Antiferromagnets, *Phys. Rev. Lett.* **119**, 187204 (2017).
- [12] Y. Zhang, J. Železný, Y. Sun, J. van den Brink, and B. Yan, Spin Hall effect emerging from a noncollinear magnetic lattice without spin-orbit coupling, *New J. Phys.* **20**, 073028 (2018).
- [13] B. A. Bernevig, C. Felser, and H. Beidenkopf, Progress and prospects in magnetic topological materials, *Nature (London)* **603**, 41 (2022).
- [14] M.-T. Suzuki, T. Koretsune, M. Ochi, and R. Arita, Cluster multipole theory for anomalous Hall effect in antiferromagnets, *Phys. Rev. B* **95**, 094406 (2017).
- [15] Y. Zhang, Y. Sun, H. Yang, J. Železný, S. P. P. Parkin, C. Felser, and B. Yan, Strong anisotropic anomalous Hall effect and spin Hall effect in the chiral antiferromagnetic compounds Mn_3X ($\text{X} = \text{Ge}, \text{Sn}, \text{Ga}, \text{Ir}, \text{Rh}, \text{and Pt}$), *Phys. Rev. B* **95**, 075128 (2017).
- [16] Y. Kobayashi, M. Kimata, D. Kan, T. Ikebuchi, Y. Shiota, H. Kohno, Y. Shimakawa, T. Ono, and T. Moriyama, Extrinsic contribution to anomalous Hall effect in chiral antiferromagnetic (111)-oriented L12- Mn_3Ir Films, *Jpn. J. Appl. Phys.* **61**, 070912 (2022).
- [17] B. E. Zuniga-Cespedes, K. Manna, H. M. L. Noad, P.-Y. Yang, M. Nicklas, C. Felser, A. P. Mackenzie, and C. W. Hicks, Observation of an anomalous Hall effect in single-crystal Mn_3Pt , *New J. Phys.* **25**, 023029 (2022).
- [18] H. Iwaki, M. Kimata, T. Ikebuchi, Y. Kobayashi, K. Oda, Y. Shiota, T. Ono, and T. Moriyama, Large anomalous Hall effect in L12-ordered antiferromagnetic Mn_3Ir thin films, *Appl. Phys. Lett.* **116**, 022408 (2020).
- [19] O. Busch, B. Göbel, and I. Mertig, Microscopic origin of the anomalous Hall effect in noncollinear kagome magnets, *Phys. Rev. Res.* **2**, 033112 (2020).
- [20] Inorganic material database (AtomWork-adv) Japan; <https://atomwork-adv.nims.go.jp/>, National Institute for Materials Science.
- [21] T. Yamashita, H. Takizawa, T. Sasaki, K. Uheda, and T. Endo, Mn_3Sb : A new L12-type intermetallic compound synthesized under high-pressure, *J. Alloys Compd.* **348**, 220 (2003).
- [22] V. S. Goncharov and V. M. Ryzhkovskii, High-pressure synthesis and crystal structure of the new compound Mn_3Sb , *Inorg. Mater.* **41**, 557 (2005).
- [23] T. R. McGuire and R. J. Happel, The magnetic susceptibility of an MnO single crystal, *J. Phys. Radium* **20**, 424 (1959).
- [24] M. Tanaka, Y. Katsuya, and A. Yamamoto, A new large radius imaging plate camera for high-resolution and high-throughput synchrotron x-ray powder diffraction by multiexposure method, *Rev. Sci. Instrum.* **79**, 075106 (2008).
- [25] M. Tanaka, Y. Katsuya, Y. Matsushita, and O. Sakata, Development of a synchrotron powder diffractometer with a one-dimensional x-ray detector for analysis of advanced materials, *J. Ceram. Soc. Jpn.* **121**, 287 (2013).
- [26] H. M. Rietveld, A profile refinement method for nuclear and magnetic structures, *J. Appl. Crystallogr.* **2**, 65 (1969).

- [27] F. Izumi and T. Ikeda, A Rietveld-analysis program RIETAN-98 and its applications to zeolites, *Mater. Sci. Forum* **321–324**, 198 (2000).
- [28] G. Kresse and J. Furthmüller, Efficient iterative schemes for ab initio total-energy calculations using a plane-wave basis set, *Phys. Rev. B* **54**, 11169 (1996).
- [29] J. P. Perdew, K. Burke, and M. Ernzerhof, Generalized Gradient Approximation Made Simple, *Phys. Rev. Lett.* **77**, 3865 (1996).
- [30] N. Marzari and D. Vanderbilt, Maximally localized generalized Wannier functions for composite energy bands, *Phys. Rev. B* **56**, 12847 (1997).
- [31] I. Souza, N. Marzari, and D. Vanderbilt, Maximally localized Wannier functions for entangled energy bands, *Phys. Rev. B* **65**, 035109 (2001).
- [32] G. Pizzi, V. Vitale, R. Arita, S. Blügel, F. Freimuth, G. Géranton, M. Gibertini, D. Gresch, C. Johnson, T. Koretsune, J. Ibañez-Azpiroz, H. Lee, J.-M. Lihm, D. Marchand, A. Marrazzo, Y. Mokrousov, J. I. Mustafa, Y. Nohara, Y. Nomura, L. Paulatto *et al.*, WANNIER90 as a community code: New features and applications, *J. Phys.: Condens. Matter* **32**, 165902 (2020).
- [33] X. Wang, J. R. Yates, I. Souza, and D. Vanderbilt, *Ab initio* calculation of the anomalous Hall conductivity by Wannier interpolation, *Phys. Rev. B* **74**, 195118 (2006).
- [34] T. Yamaoka, Antiferromagnetism in γ -phase Mn-Ir alloys, *J. Phys. Soc. Jpn.* **36**, 445 (1974).
- [35] S. Tomiyoshi and Y. Yamaguchi, Magnetic structure and weak ferromagnetism of Mn_3Sn studied by polarized neutron diffraction, *J. Phys. Soc. Jpn.* **51**, 2478 (1982).
- [36] S. Tomiyoshi, Polarized neutron diffraction study of the spin structure of Mn_3Sn , *J. Phys. Soc. Jpn.* **51**, 803 (1982).
- [37] E. Krén and G. Kádár, Neutron diffraction study of Mn_3Ga , *Solid State Commun.* **8**, 1653 (1970).
- [38] See Supplemental Material at <http://link.aps.org/supplemental/10.1103/PhysRevB.108.075140> for more information on the temperature dependence of lattice parameters, isothermal magnetization, Hall resistivity, and Hall conductivity, and a comparison with the band structures of Mn_3Sb and Mn_3Ir , as well as the relationship between Hall conductivity and universal scaling in Mn_3Sb .
- [39] V. M. Ryzhkovskii, V. S. Goncharov, S. S. Agafonov, V. P. Glazkov, V. A. Somenkov, A. P. Sazonov, and A. T. Senishin, Magnetic ordering in Mn_3Sb determined by neutron diffraction data, *J. Surf. Invest.: X-Ray, Synchrotron Neutron Tech.* **5**, 109 (2011).
- [40] V. S. Goncharov and V. M. Ryzhkovskii, Phase separation of Mn_2Sb at high pressures and temperatures, *Inorg. Mater.* **47**, 1298 (2011).
- [41] M. K. Wilkinson, N. S. Gingrich, and C. G. Shull, The magnetic structure of Mn_2Sb , *J. Phys. Chem. Solids* **2**, 289 (1957).
- [42] Y. Yao, L. Kleinman, A. H. MacDonald, J. Sinova, T. Jungwirth, D. S. Wang, E. Wang, and Q. Niu, First Principles Calculation of Anomalous Hall Conductivity in Ferromagnetic bcc Fe, *Phys. Rev. Lett.* **92**, 037204 (2004).
- [43] Z. H. Liu, Y. J. Zhang, G. D. Liu, B. Ding, E. K. Liu, H. M. Jafri, Z. P. Hou, W. H. Wang, X. Q. Ma, and G. H. Wu, Transition from anomalous Hall effect to topological Hall effect in hexagonal non-collinear magnet Mn_3Ga , *Sci. Rep.* **7**, 515 (2017).
- [44] M. Budzyński, V. S. Goncharov, V. I. Mitsiuk, Z. Surowiec, and T. M. Tkachenka, Mössbauer study of cubic phase in the Mn-Sb system, *Acta Phys. Pol. A* **125**, 850 (2014).
- [45] E. Krén, G. Kádár, L. Pál, J. Sólyom, P. Szabó, and T. Tarnóczy, Magnetic structures and exchange interactions in the Mn-Pt system, *Phys. Rev.* **171**, 574 (1968).
- [46] A. Sakuma, R. Y. Umetsu, and K. Fukamichi, Magnetic structures and their stability in Mn_3Rh ordered and disordered alloys, *Phys. Rev. B* **66**, 014432 (2002).
- [47] I. Tomeno, H. N. Fuke, H. Iwasaki, M. Sahashi, and Y. Tsunoda, Magnetic neutron scattering study of ordered Mn_3Ir , *J. Appl. Phys.* **86**, 3853 (1999).
- [48] V. S. Goncharov and S. V. Trukhanov, Triangular magnetic structure of the Mn_3Sb Compound, *Proc. Natl. Acad. Sci. Belarus. Phys. Math. Ser.* **56**, 232 (2020).
- [49] A. P. Vokhmyanin, A. S. Gritsai, and V. M. Ryzhkovskii, Symmetry analysis of the magnetic structure of Mn_3Sb , *Phys. Met. Metall.* **113**, 756 (2012).
- [50] T. Yamaoka, M. Mekata, and H. Takaki, Neutron diffraction study of γ -phase Mn-Ir single crystals, *J. Phys. Soc. Jpn.* **36**, 438 (1974).
- [51] S. Onoda, N. Sugimoto, and N. Nagaosa, Intrinsic versus Extrinsic Anomalous Hall Effect in Ferromagnets, *Phys. Rev. Lett.* **97**, 126602 (2006).
- [52] H.-W. Bang, W. Yoo, C. Kim, S. Lee, J. Gu, Y. Park, K. Lee, and M.-H. Jung, Structural, magnetic, and electrical properties of collinear antiferromagnetic heteroepitaxy cubic Mn_3Ga thin films, *Appl. Phys. Lett.* **115**, 012402 (2019).